

## MMS Observations of a Compressed Current Sheet: Importance of the Ambipolar Electric Field

Ami M. DuBois<sup>1</sup>, Chris Crabtree<sup>1</sup>, Gurudas Ganguli<sup>1</sup>, David M. Malaspina<sup>2,3</sup>, and William E. Amatucci<sup>1</sup>

<sup>1</sup>*U.S. Naval Research Laboratory, Plasma Physics Division, Washington, D.C. 20375-5346, USA*

<sup>2</sup>*Astrophysical and Planetary Sciences Department, University of Colorado, Boulder, Colorado 80303-7814, USA*

<sup>3</sup>*Laboratory for Atmospheric and Space Physics, University of Colorado, Boulder, Colorado 80303-7814, USA*



(Received 13 December 2021; revised 15 July 2022; accepted 12 August 2022;  
published 2 September 2022; corrected 6 September 2022)

Spacecraft data reveal a nonuniform ambipolar electric field transverse to the magnetic field in a thin current sheet in Earth's magnetotail that leads to intense  $\mathbf{E} \times \mathbf{B}$  velocity shear and nongyrotropic particle distributions. The  $\mathbf{E} \times \mathbf{B}$  drift far exceeds the diamagnetic drift and thus drives observed lower hybrid waves. The shear-driven waves are localized to the magnetic field reversal region and are therefore ideally suited for the anomalous dissipation necessary for reconnection. It also reveals substructures embedded in the current density, indicating a compressed current sheet.

DOI: [10.1103/PhysRevLett.129.105101](https://doi.org/10.1103/PhysRevLett.129.105101)

Current sheets are important to space and laboratory plasmas [1–6], and particularly to Earth's magnetotail. A consequential but overlooked feature of thin current sheets is a transverse ambipolar electric field which is self-consistently generated as the magnetotail is compressed by the solar wind [7]. This interaction of large and small-scale physics may consist of turbulent processes forming plasmoids and flux ropes, etc. [8,9] with kinetic-scale current sheets between them that can reorganize the macroscopic magnetic topology through reconnection and affect the magnetospheric plasma environment, also known as “space weather.” *In situ* measurements have shown compression of the magnetotail creates thin current sheets of widths comparable to the ion gyroradius ( $\rho_i$ ), occasionally with single [10–12] or double peaked [13–17] substructures embedded in the current density. These thin structured current sheets cannot be explained by the standard Harris equilibrium [18], which is commonly used as an ideal current sheet representation [6]. Intense lower hybrid (LH) wave activity and subsequent magnetic reconnection with large scale topological changes is also observed, which may result in a plasma dipolarization front accelerating toward Earth, injecting energetic particles into the radiation belts [19–24], followed by a redistribution of mass, energy, and momentum throughout the magnetosphere [6,7,16,25–28] which impacts Earth orbiting satellites. It is therefore critical to understand the physics of thin structured current sheets, especially the kinetic structures within, and the associated dynamics. The formation of the ambipolar electric field in thin current sheets at the smallest scale can affect particle orbits and provides a new mechanism to generate intense electrostatic turbulence near the magnetic field reversal, resulting in anomalous dissipation processes that can initiate magnetic reconnection.

Theoretical [7,29,30] and laboratory [31–33] studies have shown that velocity shear can intensify due to the ambipolar electric field generated by plasma compression, driving broadband turbulence peaking at the LH frequency. Shear-driven LH waves dominate over the LH drift (LHD) instability at the center of the current sheet where the density is nearly flat [34] and the shear frequency, defined as the spatial derivative of the  $\vec{E} \times \vec{B}$  flow, exceeds the diamagnetic drift frequency [7,35,36]. Identification of shear-driven LH waves in *in situ* data is not only evidence of a thin structured current sheet, but also emphasizes the importance of the ambipolar electric field [7], the scope of which has not been explored in previous magnetotail investigations [37–42]. As the scale size of the current sheet becomes comparable to  $\rho_i$ , the electric field intensifies making the velocity shear strong, which can explain many observed features and their causality, such as nongyrotropic distributions [7,16,28,43,44], plasma heating and cooling [7,27,41], vortex structures [7,20,35,45,46], and the wide bandwidth of spectral signatures [7,32]. The ability of the ambipolar electric field to break gyrotropy is an indicator of its major role in reconnection [47–49]. This Letter presents the first evidence of shear-driven LH waves resulting from global compression that demonstrates the significance of transverse ambipolar electric fields in thin current sheets that can occur prior to reconnection.

The four Magnetospheric Multiscale (MMS) spacecraft [50] traversed a current sheet (an approximate 1D plasma structure near a magnetic reversal) in Earth's magnetotail on July 3, 2017 and crossed the null point at approximately 5:27:07.02 UTC. Rotating the vector data into a frame normal to the current sheet (LMN coordinates) allows for the analysis below, which suggests that an ambipolar electric field forms due to compression of the current

sheet, with an  $\vec{E} \times \vec{B}$  shear flow associated with LH fluctuations. The density gradient is small in this region, suggesting that the shear flow provides the energy for the fluctuations.

During this event, the MMS spacecraft are in the night side of Earth's plasma sheet on the dusk side of midnight far from the magnetopause. Using the magnetic field measurements between 6 and 8 s, minimum variance analysis (MVA) [51,52] is used to calculate the eigenvector corresponding to a direction normal ( $\hat{N}$ ) to the current sheet. The angular difference between the averaged eigenvector and the eigenvectors calculated individually from each spacecraft [ $\cos^{-1}(\hat{n}_{\text{avg}} \cdot \hat{n}_i)$ ] is small ( $<4^\circ$ ), which is a good indicator that the magnetic field gradient is much stronger in  $\hat{N}$  compared to other directions. Additionally, a guide for judging the quality of the MVA is a large ratio of the eigenvalues corresponding to the  $\hat{M}$  and  $\hat{N}$  directions ( $\lambda_M/\lambda_N = 12$ ), indicating a well-defined  $\hat{N}$  direction [51]. The resulting transformation matrix from GSE coordinates is  $[L, M, N] = [[-0.67, -0.68, -0.30], [-0.70, 0.71, -0.04], [-0.24, -0.18, 0.95]]$ . The vector data presented henceforth are rotated into LMN coordinates using the transformation matrix in order to better infer measurements with respect to the orientation of the current sheet such that  $\hat{N}$  is normal to the current sheet,  $\hat{L}$  is in the direction whose magnetic component reverses sign, and  $\hat{M}$  is the direction of the guide magnetic field.

A summary of the MMS1 data for a 5 s time span during the current sheet crossing is shown in Fig. 1. Data from each spacecraft are comparable with similar features, so only MMS1 data are shown. A boxcar averaging low pass filter routine is applied to the time series measurements to improve the signal to noise ratio and smooth the data to infer quasistatic profiles. The top axis displays time converted to distance and normalized to a representative  $\rho_i$  (calculated from the average of the total magnetic field and ion temperature between 7 and 8 s) to show how features compare to ion-scale sizes. To convert time to distance, we use the fact that the current sheet is sweeping by in  $\hat{N}$  much faster than the spacecraft are moving ( $V_{\text{MMS}} = 1.47$  km/s). The magnetic field data from each spacecraft are shifted in time to align the  $B_L$  reversals. With the timing information and the spacecraft locations relative to each other, the current sheet velocity can be estimated as  $V_{cs} = 223.1 \pm 57.5$  km/s  $\hat{N}$ . The time ( $x$  axis) is then multiplied by  $V_{cs}$  to convert to distance, and then normalized to  $\rho_i$ .

The magnetic field LMN components in Fig. 1(a) show that by rotating the data into a frame normal to the current sheet,  $B_N$  is near zero with a  $B_L$  reversal at 7.02 s (dashed, vertical line), which indicates the current sheet crossing. The measured quantities are not symmetric about the  $B_L$  reversal. There is a guide field ( $B_M$ ) of approximately 10 nT at the time of  $B_L$  reversal. Using the average total magnetic

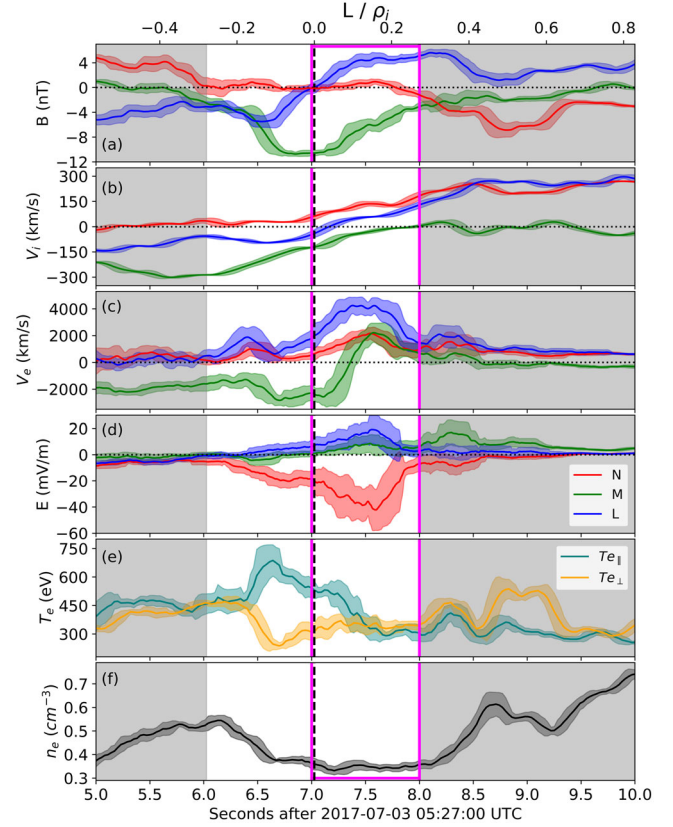


FIG. 1. Boxcar averaged MMS1 plasma parameters as a function of time (bottom axis) and distance normalized to  $\rho_i = 841$  km (top axis). (a) Magnetic field burst data (128 S/s) measured by the fluxgate magnetometer [54], (b) ion velocity, (c) electron velocity, and (d) electric field burst data (8192 S/s) measured by FIELDS [53] rotated into LMN coordinates (blue =  $\hat{L}$ , green =  $\hat{M}$ , red =  $\hat{N}$ ), (e) parallel (teal) and perpendicular (orange) electron temperature, and (f) electron density. Velocities, densities, and temperatures are obtained from the fast plasma investigation (FPI) [55] burst measurements (ions = 6 S/s, electrons = 33 S/s). The unshaded region highlights  $\pm 1$  second around the  $B_L$  reversal (vertical dashed line), around which the electron diffusion region is typically located. The magenta box indicates the region during which electrostatic LH fluctuations are present.

field between 7 and 8 s (magenta box),  $\rho_i = 841$  km and  $\rho_e = 6.9$  km (electron gyroradius). The ion velocity [Fig. 1(b)] is significantly smaller than the electron velocity [Fig. 1(c)], indicating that the ions experience negligible electric field due to gyro averaging as the electric field scale size is less than  $\rho_i$  [7]. The total electron flow velocity ( $V_{eL}$ ) has a scale size less than  $\rho_i$ . The electric field components are shown in Fig. 1(d), where  $E_L$  and  $E_M$  are both small compared to  $E_N$  (ambipolar electric field normal to the current sheet), which has a scale size less than  $\rho_i$  and peaks at  $-45$  mV/m. The electron temperatures ( $T_e$ ) and density ( $n_e$ ) are shown in Figs. 1(e) and 1(f). In the region of peak  $E_N$ ,  $n_e$  is nearly constant but exhibits a gradient at approximately 6.5 and 8.5 s.

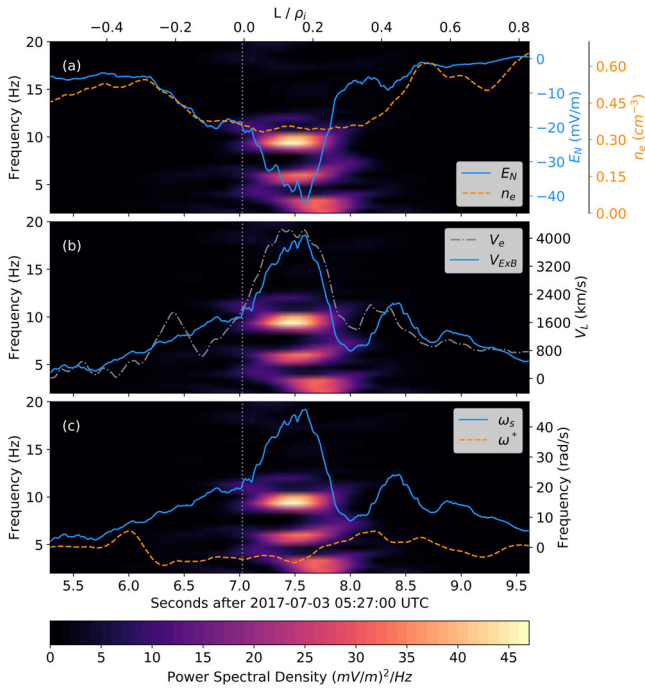


FIG. 2. Spectrogram showing power spectral density of electrostatic LH fluctuations as a function of time with (a)  $E_N$  (solid, blue) and  $n_e$  (dashed, orange), (b) total electron (gray, dot-dashed) and  $\vec{E} \times \vec{B}$  shear (blue, solid) velocities in  $\hat{L}$ , (c) shear (blue, solid) and diamagnetic drift (dashed, orange) frequencies overlaid. The top axis shows distance normalized to  $\rho_i$ . The vertical dotted line indicates the  $B_L$  reversal time.

Electrostatic fluctuation spectra are calculated by taking a spectrogram [52] of the  $E_N$  burst measurement data prior to boxcar averaging. All panels in Fig. 2 show electrostatic fluctuations from 2 to 20 Hz, where color specifies the power spectral density such that black indicates instrument noise level and yellow indicates large amplitude fluctuations. The LH frequency [ $f_{LH} = (1/2\pi)\sqrt{\omega_{ci}\omega_{ce}}$ ] at the  $B_L$  reversal is 7 Hz. The peak fluctuations occur at 7.5 s with a frequency of approximately 10 Hz, indicating these are LH waves. The boxcar averaged  $E_N$  (solid, blue) and  $n_e$  (dashed, orange) are overlaid on the fluctuation spectra [Fig. 2(a)] showing that  $E_N$  peaks during the largest amplitude fluctuations. The  $n_e$  is nearly constant during the time of fluctuations, and when there is a gradient, no LH fluctuations are observed. There is a large  $\vec{E} \times \vec{B}$  velocity shear in  $\hat{L}$  direction [Fig. 2(b), solid blue], where the wave activity peaks. The total electron flow in  $\hat{L}$ ,  $V_{eL}$  [Fig. 2(b), gray dot-dashed], is in the same direction as  $V_{E \times B}$ , indicating that the electrons are  $\vec{E} \times \vec{B}$  drifting. Additionally, because  $V_{eL}$  and  $V_{E \times B}$  are close in magnitude, the diamagnetic drift velocity [ $\vec{V}_{\text{drift}} = \nabla P_e \times \vec{B} / (n_e B^2)$ ] in the region of the wave localization is small compared to the  $\vec{E} \times \vec{B}$  velocity.

This indicates that the LH waves are driven by the sheared flow and not a density gradient.

The origin of the observed features can be gleaned from our kinetic model [7,56], which is extended to include a guide field. Although the model includes magnetic field components in the  $y$  and  $z$  directions, it uses a WKB type ansatz, incorporating the strongest observed variation in the  $x$  direction, perpendicular to the magnetic field. It constructs an exact solution to the Vlasov-Maxwell equations for species  $\alpha$  by generalizing the Harris model to include an inhomogeneous guiding-center distribution,

$$f_{0\alpha} = \frac{N_{0\alpha}}{(\pi v_{T\alpha}^2)^{3/2}} Q_\alpha(\Upsilon_\alpha, \zeta_\alpha) \times e^{-[E_\alpha - U_\alpha p_y - V_\alpha p_z + (1/2)m_\alpha U_\alpha^2 + (1/2)m_\alpha V_\alpha^2]/T_\alpha}, \quad (1)$$

where  $Q_\alpha(\Upsilon_\alpha, \zeta_\alpha) = G(\Upsilon_\alpha) + H(\zeta_\alpha)$ ,

$$G(\Upsilon_\alpha) = \frac{1}{2} \left[ R_{y\alpha} + S_{y\alpha} + (S_{y\alpha} - R_{y\alpha}) \operatorname{erf} \left( \frac{\Upsilon_\alpha - \Upsilon_0}{L_{y\alpha}} \right) \right],$$

$$H(\zeta_\alpha) = R_{z\alpha} + (S_{z\alpha} - R_{z\alpha}) \exp \left( -\frac{(\zeta_\alpha - \zeta_0)^2}{L_{z\alpha}^2} \right),$$

$\Upsilon_\alpha = [A_y(x)/B_0 + v_y/\Omega_\alpha]$  and  $\zeta_\alpha = [A_z(x)/B_0 - B_v x + v_z/\Omega_\alpha]$  are the canonical momenta,  $N_{0\alpha} S_\alpha$  and  $N_{0\alpha} R_\alpha$  are asymptotic densities on the high or low sides of the guiding center distributions,  $G$  and  $H$ , and  $B_v$  is the vacuum component (due to external currents) of the guide field. The quasineutrality condition gives the electrostatic potential and Ampere's law gives the vector potential. This fully specifies the distribution function and allows inhomogeneous structures in the moments (e.g., density, current, temperature, flows) to self-consistently develop in response to compression, which is represented by the scale sizes  $L_{y\alpha}$  and  $L_{z\alpha}$  of  $G$  and  $H$ , similar to the case with no guide field described in [7]. The current sheet evolves on slow fluid timescales under compression, but the instability (Fig. 4) timescale is much faster. Hence, a stationary Vlasov solution is a reasonable assumption for understanding the wave effects. However, a simulation initialized by Eq. (1) can provide a more accurate picture of the dynamics. Using the parameters provided in Supplemental Material [52], Fig. 3 compares MMS1 data (dashed, blue) to the model (solid, red) for (a)  $B_L$ , (b)  $V_{iL}$ , (c)  $V_{eL}$ , (d)  $E_N$ , and (e) electron current density in  $\hat{L}$ . It shows that as a broad Harris-type current sheet undergoes global compression, an ambipolar electric field ( $E_N$ ) self-consistently develops. This produces a sheared  $\vec{E} \times \vec{B}$  velocity, enabling shear-driven waves to arise in thin current sheets. The presence of a guide magnetic field introduces sheared parallel flows,  $V_{\parallel} = (\vec{E} \times \vec{B})/B^2 \cdot \hat{b}_{L,M}$ , which can also drive waves [7]. Additionally, the bidirectional  $V_{iL}$  flow profile is found to be a stationary Vlasov solution

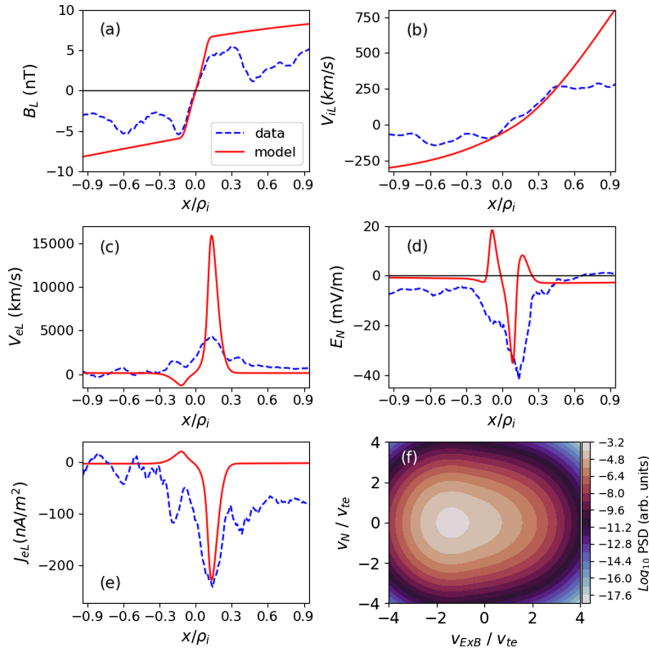


FIG. 3. Kinetic equilibrium model (solid, red) compared to MMS data (dashed, blue) as a function of distance normalized to  $\rho_i$  for (a) magnetic field in  $\hat{L}$ , (b) ion velocity in  $\hat{L}$ , (c) electron velocity in  $\hat{L}$ , (d) ambipolar electric field in  $\hat{N}$ , (e) electron current density in  $\hat{L}$ . (f) The modeled nongyrotropic electron distribution function that arises due to the ambipolar electric field, where the axes represent the electron flow in the direction of  $E_N$  (vertical) and parallel to  $V_{E \times B}$  (horizontal) normalized to the thermal velocity. The color bar represents the log of the phase space density in arbitrary units.

and therefore may not imply occurrence of magnetic reconnection, as claimed [20]. Given the boundary conditions from the *in situ* measurements, the equilibrium model agrees with the general trends of the measurements. The observed profiles are relaxed because of the instability.

Our model also shows that as current sheets are compressed to scales less than  $\rho_i$ , substructures embedded in the current density can form, which cannot be explained by the standard Harris equilibrium. The current density ( $J$ ) is calculated from MMS FPI data ( $\vec{J} = en_i \vec{V}_i - en_e \vec{V}_e$ ), where the electron term dominates ( $V_i \ll V_e$ ). Since  $B_M > B_L$ , the electron current density in  $\hat{L}$ ,  $J_{eL}$ , is dominant and is comparable to the cross-field Hall current,  $J \approx en(E_N \times B_M)$ . Figure 3(e) shows the  $J_{eL}$  data (dashed, blue) and model (solid, red). The large peak in  $J_{eL}$  is localized to the region of  $E_N$  and the waves. Both the data and model suggest the formation of a thin current sheet that has substructures contained within.

A distinguishing property of our equilibrium model is the formation of agyrotropy in distribution functions [7], which has been seen in this event but was thought to be a wave heating effect [20]. Figure 3(f) shows the electron distribution function from the model, where the vertical

axis is the electron flow in the direction along  $E_N$  and the horizontal axis is the direction of  $V_{E \times B}$ , both normalized to the thermal velocity. The agyrotropy arises in the equilibrium distribution function due to the ambipolar electric field.

Velocity shear can drive LH waves even in the presence of a pressure gradient as long as the shear frequency ( $\omega_s \sim |\vec{V}_{E \times B}|/L_E$ ) is greater than the diamagnetic drift frequency ( $\omega^* = -k_\perp \vec{V}_{\text{drift}}$ ) [7,29,35,36,56]. The shear scale length ( $L_E$ ) can be estimated by taking the half-width at half-max of the boxcar averaged  $E_N$ . The average  $L_E$  is estimated to be  $89 \pm 23$  km such that  $\rho_e < L_E < \rho_i$ . Following Norgren *et al.* [46],  $k_\perp$  is calculated by first finding the time shift between  $E_L$  measured from MMS1 and MMS2 (largest separation in  $\hat{L}$ ). The wave phase speed is calculated using the distance in  $\hat{L}$  between MMS1 and MMS2 and the time shift between the signals. The phase speed is then used to calculate the fluctuation wavelength,  $k_\perp = (2\pi/\lambda) = 0.027 \pm 0.01$  km $^{-1}$ . Figure 2(c) shows that  $\omega_s$  (blue, solid) is an order of magnitude larger than  $\omega^*$  (orange, dashed), indicating that the velocity shear is the dominating energy source for the waves. The electron-ion hybrid (EIH) instability is driven by the free energy provided by sheared flows [7,33,36,57] and characterized by  $k_\perp \rho_e \ll 1$  and  $k_\perp L_E \sim 1$ . Observations from this event give  $k_\perp \rho_e = 0.18 \pm 0.07$  and  $k_\perp L_E = 2.4 \pm 1.2$  reinforcing that the character of the LH fluctuations are consistent with EIH instability and not the LHD instability. Vortices, reported earlier for this event [20], are also a natural consequence of the velocity shear that drives the EIH waves [35].

In order to compare this dataset with theory, we generalized the nonlocal theory of the EIH instability [58] to include a guide field and magnetic field reversal. A model equilibrium electric field, consistent with the observed  $E_N$ , is used to drive sheared flows in  $V_L$  and  $V_M$ . The parameters [52] used to solve the eigenvalue problem are consistent with observations. The eigenfunction corresponding to the EIH mode with the maximum growth rate is localized around the strong  $V_L$  flow near the center of the current sheet [Fig. 4(a)], also consistent with observations. Solution of the eigenmode condition as a function of  $k_L$  normalized by  $L_E$  provides the growth rate and frequency [Fig. 4(b)] normalized to  $\omega_{LH}$ , indicating a large domain of the shear driven instability ideally located in the center of the current sheet for anomalous dissipation [35,59,60] to trigger reconnection.

In summary, *in situ* measurements show a localized ambipolar electric field develops in a thin current sheet and results in a strong sheared  $\vec{E} \times \vec{B}$  velocity, which drives LH fluctuations, with a negligible density gradient. The ambipolar electric field breaks gyrotropy in the distribution function and drives waves capable of producing anomalous resistivity that can determine the reconnection rate.

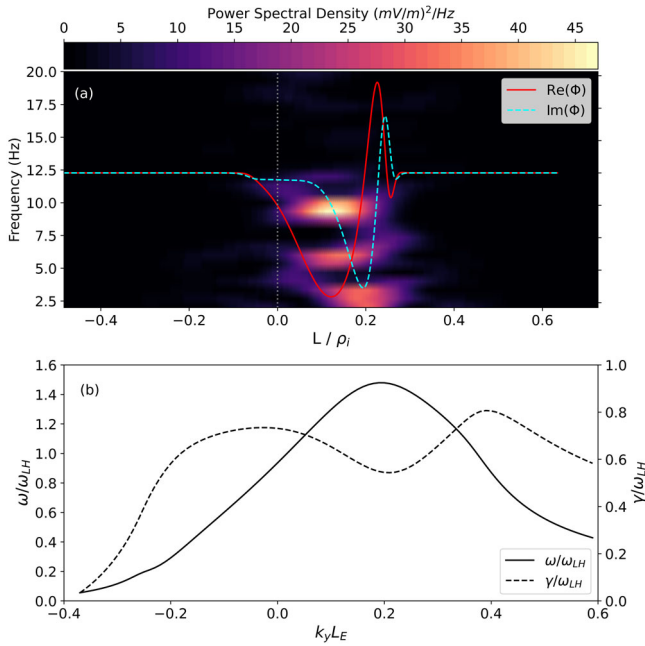


FIG. 4. (a) Spectrogram showing power spectral density of electrostatic LH fluctuations as a function of distance normalized to  $\rho_i$  with the real (solid, red) and imaginary (dashed, blue) eigenmodes,  $\phi$ , overlaid. The vertical dotted line indicates the  $B_L$  reversal. (b) The frequency (solid) and growth rate (dashed) normalized to  $\omega_{LH}$  plotted as a function of  $k_y L_E$ .

This implies a seamless connection of the local reconnection rate with the global compression. With further research, it will be possible to develop a parametrization of the anomalous resistivity suitable for fluid models to trigger reconnection for realistic parameters consistent with global forcing. Since 3D PIC simulations with large scales and mass ratios needed to capture the essential physics are expensive, fluid models with a parametrization of the kinetic effects is an optimal way to explore the larger-scale physics with local kinetic feedback.

The frozen-in condition may be broken by anomalous resistivity. However, the off-diagonal terms in the pressure tensor can also play a role [42,61,62]. Interestingly, off-diagonal terms may also be generated by compression, as was argued for dipolarization fronts [63]. Using our kinetic equilibrium as the initial condition in PIC simulations could help reveal the impact of thin structured current sheets and the associated dynamics on reconnection, and the relative roles of anomalous resistivity and off-diagonal components of the pressure tensor. These are interesting topics for further research.

All MMS data used in this Letter are publically available and can be found online at the MMS Science Data Center.

This work was supported by the Naval Research Laboratory Base Program.

- [1] M. Yamada, R. Kulsrud, and H. Ji, Magnetic reconnection, *Rev. Mod. Phys.* **82**, 603 (2010).
- [2] J. Chen, Physics of the magnetotail current sheet, *Phys. Fluids B* **5**, 2663 (1993).
- [3] C. Chen, Y.D. Liu, and H. Hu, Macro magnetic holes caused by ripples in heliospheric current sheet from coordinated imaging and Parker Solar Probe observations, *Astrophys. J.* **921**, 1 (2021).
- [4] L. P. Chitta, E. R. Priest, and X. Cheng, From formation to disruption: Observing the multiphase evolution of a solar flare current sheet, *Astrophys. J.* **911**, 133 (2021).
- [5] L. B. Wilson, A. L. Brosius, N. Gopalswamy, T. Nieves-Chinchilla, A. Szabo, K. Hurley, T. Phan, J. C. Kasper, N. Lugaz, I. G. Richardson, C. H. K. Chen, D. Verscharen, R. T. Wicks, and J. M. TenBarge, A quarter century of wind spacecraft discoveries, *Rev. Geophys.* **59**, 1 (2021).
- [6] A. Petrukovich, A. Artemyev, I. Vasko, R. Nakamura, and L. Zelenyi, Current sheets in the Earth magnetotail: Plasma and magnetic field structure with cluster project observations, *Space Sci. Rev.* **188**, 311 (2015).
- [7] G. Ganguli, C. Crabtree, A. Fletcher, and B. Amatucci, Behavior of compressed plasmas in magnetic fields, *Rev. Mod. Plasma Phys.* **4**, 1 (2020).
- [8] D. A. Uzdensky, N. F. Loureiro, and A. A. Schekochihin, Fast Magnetic Reconnection in the Plasmoid-Dominated Regime, *Phys. Rev. Lett.* **105**, 235002 (2010).
- [9] W. Daughton, V. Roytershteyn, H. Karimabadi, L. Yin, B. J. Albright, B. Bergen, and K. J. Bowers, Role of electron physics in the development of turbulent magnetic reconnection in collisionless plasmas, *Nat. Phys.* **7**, 539 (2011).
- [10] D. J. McComas, C. T. Russell, R. C. Elphic, and S. J. Bame, The near-Earth cross-tail current sheet: Detailed ISEE 1 and 2 case studies, *J. Geophys. Res.* **91**, 4287 (1986).
- [11] A. A. Petrukovich, A. V. Artemyev, H. V. Malova, V. Y. Popov, R. Nakamura, and L. M. Zelenyi, Embedded current sheets in the Earth's magnetotail, *J. Geophys. Res.* **116**, A00I25 (2011).
- [12] V. I. Domrin, H. V. Malova, A. V. Artemyev, and A. P. Kropotkin, Peculiarities of the formation of a thin current sheet in the Earth's magnetosphere, *Cosmic Res. (Transl. of Kosm. Issled.)* **54**, 423 (2016).
- [13] K. Schindler and M. Hesse, Formation of thin bifurcated current sheets by quasisteady compression, *Phys. Plasmas* **15**, 042902 (2008).
- [14] M. Hoshino, A. Nishida, T. Mukai, Y. Saito, T. Yamamoto, and S. Kokubun, Structure of plasma sheet in magnetotail: Double-peaked electric current sheet, *J. Geophys. Res.* **101**, 24775 (1996).
- [15] Y. Asano, T. Mukai, M. Hoshino, Y. Saito, H. Hayakawa, and T. Nagai, Current sheet structure around the near-Earth neutral line observed by geotail, *J. Geophys. Res.* **109**, 1 (2004).
- [16] C. Norgren, D. B. Graham, Y. V. Khotyaintsev, M. André, A. Vaivads, M. Hesse, E. Eriksson, P. A. Lindqvist, B. Lavraud, J. Burch, S. Fuselier, W. Magnes, D. J. Gershman, and C. T. Russell, Electron reconnection in the magnetopause current layer, *J. Geophys. Res.* **123**, 9222 (2018).
- [17] A. Runov, R. Nakamura, W. Baumjohann, T. L. Zhang, M. Volwerk, H. U. Eichelberger, and A. Balogh, Cluster

- observation of a bifurcated current sheet, *Geophys. Res. Lett.* **30**, 1036 (2003).
- [18] E. G. Harris, On a plasma sheath separating regions of oppositely directed magnetic field, *Nuovo Cimento (1955–1965)* **23**, 115 (1962).
- [19] D. A. Gurnett, L. A. Frank, and R. P. Lepping, Plasma waves in the distant magnetotail, *J. Geophys. Res.* **81**, 6059 (1976).
- [20] L. J. Chen *et al.*, Lower-Hybrid Drift Waves Driving Electron Nongyrotropic Heating and Vortical Flows in a Magnetic Reconnection Layer, *Phys. Rev. Lett.* **125**, 025103 (2020).
- [21] S. Ohtani, H. Korth, P. C. Brandt, L. G. Blomberg, H. J. Singer, M. G. Henderson, E. A. Lucek, H. U. Frey, Q. Zong, J. M. Weygand, Y. Zheng, and A. T. Y. Lui, Cluster observations in the inner magnetosphere during the 18 April 2002 Sawtooth event: Dipolarization and injection at  $r = 4.6$  RE, *J. Geophys. Res.* **112**, A08213 (2007).
- [22] R. Nakamura, W. Baumjohann, Y. Asano, A. Runov, A. Balogh, C. J. Owen, A. N. Fazakerley, M. Fujimoto, B. Klecker, and H. Rème, Dynamics of thin current sheets associated with magnetotail reconnection, *J. Geophys. Res.* **111**, A11206 (2006).
- [23] M. Nosé, H. Koshiishi, H. Matsumoto, P. Cson Brandt, K. Keika, K. Koga, T. Goka, and T. Obara, Magnetic field dipolarization in the deep inner magnetosphere and its role in development of  $O^+$ -rich ring current, *J. Geophys. Res.* **115**, A00J03 (2010).
- [24] Y. Xu, H. S. Fu, C. Norgren, K. J. Hwang, and C. M. Liu, Formation of dipolarization fronts after current sheet thinning, *Phys. Plasmas* **25**, 072123 (2018).
- [25] R. Nakamura, W. Baumjohann, A. Runov, M. Volwerk, T. L. Zhang, B. Klecker, Y. Bogdanova, A. Roux, A. Balogh, H. Rème, J. A. Sauvaud, and H. U. Frey, Fast flow during current sheet thinning, *Geophys. Res. Lett.* **29**, 2140 (2002).
- [26] Y. Asano, T. Mukai, M. Hoshino, Y. Saito, H. Hayakawa, and T. Nagai, Statistical study of thin current sheet evolution around substorm onset, *J. Geophys. Res.* **109**, 1 (2004).
- [27] J. Liang, W. W. Liu, and E. F. Donovan, Ion temperature drop and quasi-electrostatic electric field at the current sheet boundary minutes prior to the local current disruption, *J. Geophys. Res.* **114**, A10215 (2009).
- [28] S. Lu *et al.*, Magnetotail reconnection onset caused by electron kinetics with a strong external driver, *Nat. Commun.* **11**, 5049 (2020).
- [29] G. Ganguli, M. J. Keskinen, H. Romero, R. Heelis, T. Moore, and C. Pollock, Coupling of microprocesses and macroprocesses due to velocity shear: An application to the low-altitude ionosphere, *J. Geophys. Res.* **99**, 8873 (1994).
- [30] H. Romero and G. Ganguli, Relaxation of the stressed plasma sheet boundary layer, *Geophys. Res. Lett.* **21**, 645 (1994).
- [31] A. M. DuBois, E. Thomas, Jr., W. E. Amatucci, and G. Ganguli, Plasma Response to a Varying Degree of Stress, *Phys. Rev. Lett.* **111**, 145002 (2013).
- [32] A. M. DuBois, E. Thomas, W. E. Amatucci, and G. Ganguli, Experimental characterization of broadband electrostatic noise due to plasma compression, *J. Geophys. Res.* **119**, 5624 (2014).
- [33] W. E. Amatucci, G. Ganguli, D. N. Walker, G. Gatling, M. Balkey, and T. McCulloch, Laboratory investigation of boundary layer processes due to strong spatial inhomogeneity, *Phys. Plasmas* **10**, 1963 (2003).
- [34] A. Runov, V. A. Sergeev, R. Nakamura, W. Baumjohann, S. Apatenkov, Y. Asano, T. Takada, M. Volwerk, Z. Vörös, T. L. Zhang, J. A. Sauvaud, H. Rème, and A. Balogh, Local structure of the magnetotail current sheet: 2001 cluster observations, *Ann. Geophys.* **24**, 247 (2006).
- [35] H. Romero and G. Ganguli, Nonlinear evolution of a strongly sheared cross-field plasma flow, *Phys. Fluids B* **5**, 3163 (1993).
- [36] A. M. DuBois, E. Thomas, W. E. Amatucci, and G. Ganguli, Density gradient effects on transverse shear driven lower hybrid waves, *Phys. Plasmas* **21**, 062117 (2014).
- [37] M. I. Sitnov, P. N. Guzdar, and M. Swisdak, A model of the bifurcated current sheet, *Geophys. Res. Lett.* **30**, 1712 (2003).
- [38] J. Birn, K. Schindler, and M. Hesse, Thin electron current sheets and their relation to auroral potentials, *J. Geophys. Res.* **109**, A02217 (2004).
- [39] P. H. Yoon and A. T. Y. Lui, Model of ion- or electron-dominated current sheet, *J. Geophys. Res.* **109**, A11213 (2004).
- [40] M. I. Sitnov, M. Swisdak, P. N. Guzdar, and A. Runov, Structure and dynamics of a new class of thin current sheets, *J. Geophys. Res.* **111**, A08204 (2006).
- [41] W. W. Liu, J. Liang, and E. F. Donovan, Electrostatic field and ion temperature drop in thin current sheets: A theory, *J. Geophys. Res.* **115**, A03211 (2010).
- [42] J. Egedal, J. Ng, A. Le, W. Daughton, B. Wetherington, J. Dorelli, D. Gershman, and A. Rager, Pressure Tensor Elements Breaking the Frozen-In Law during Reconnection in Earth's Magnetotail, *Phys. Rev. Lett.* **123**, 225101 (2019).
- [43] M. Zhou, X. H. Deng, Z. H. Zhong, Y. Pang, R. X. Tang, M. El-Alaoui, R. J. Walker, C. T. Russell, G. Lapenta, R. J. Strangeway, R. B. Torbert, J. L. Burch, W. R. Paterson, B. L. Giles, Y. V. Khotyaintsev, R. E. Ergun, and P.-A. Lindqvist, Observations of an electron diffusion region in symmetric reconnection with weak guide field, *Astrophys. J.* **870**, 34 (2019).
- [44] R. Nakamura, K. J. Genestreti, T. Nakamura, W. Baumjohann, A. Varsani, T. Nagai, N. Bessho, J. L. Burch, R. E. Denton, J. P. Eastwood, R. E. Ergun, D. J. Gershman, B. L. Giles, H. Hasegawa, M. Hesse, P. A. Lindqvist, C. T. Russell, J. E. Stawarz, R. J. Strangeway, and R. B. Torbert, Structure of the current sheet in the 11 July 2017 electron diffusion region event, *J. Geophys. Res.* **124**, 1173 (2019).
- [45] S. Wang, L. J. Chen, J. Ng, N. Bessho, and M. Hesse, Lower-hybrid drift waves and their interaction with plasmas in a 3D symmetric reconnection simulation with zero guide field, *Phys. Plasmas* **28**, 072102 (2021).
- [46] C. Norgren, A. Vaivads, Y. V. Khotyaintsev, and M. André, Lower Hybrid Drift Waves: Space Observations, *Phys. Rev. Lett.* **109**, 055001 (2012).
- [47] S. M. Mahajan and R. D. Hazeltine, Sheared-flow generalization of the Harris sheet, *Phys. Plasmas* **7**, 1287 (2000).

- [48] J. D. Scudder and F. S. Mozer, Electron demagnetization and collisionless magnetic reconnection in  $Be \ll 1$  plasmas, *Phys. Plasmas* **12**, 092903 (2005).
- [49] J. Scudder and W. Daughton, Illuminating electron diffusion regions of collisionless magnetic reconnection using electron agyrotropy, *J. Geophys. Res.* **113**, A06222 (2008).
- [50] J. L. Burch, T. E. Moore, R. B. Torbert, and B. L. Giles, Magnetospheric multiscale overview and science objectives, *Space Sci. Rev.* **199**, 5 (2016).
- [51] R. E. Denton, B. U. Ö. Sonnerup, C. T. Russell, H. Hasegawa, T. D. Phan, R. J. Strangeway, B. L. Giles, R. E. Ergun, P. A. Lindqvist, R. B. Torbert, J. L. Burch, and S. K. Vines, Determining  $L$ - $M$ - $N$  current sheet coordinates at the magnetopause from magnetospheric multiscale data, *J. Geophys. Res.* **123**, 2274 (2018).
- [52] See Supplemental Material at <http://link.aps.org/supplemental/10.1103/PhysRevLett.129.105101> for detailed information on the minimum variance analysis (MVA), electrostatic fluctuation spectra, and the parameters used in the equilibrium model.
- [53] R. B. Torbert *et al.*, The FIELDS instrument suite on MMS: Scientific objectives, measurements, and data products, *Space Sci. Rev.* **199**, 105 (2016).
- [54] C. T. Russell *et al.*, The magnetospheric multiscale magnetometers, *Space Sci. Rev.* **199**, 189 (2016).
- [55] C. Pollock *et al.*, Fast plasma investigation for magnetospheric multiscale, *Space Sci. Rev.* **199**, 331 (2016).
- [56] A. C. Fletcher, C. Crabtree, G. Ganguli, D. Malaspina, E. Tejero, and X. Chu, Kinetic equilibrium and stability analysis of dipolarization fronts, *J. Geophys. Res.* **124**, 2010 (2019).
- [57] G. Ganguli, Y. C. Lee, and P. J. Palmadesso, Electron-ion hybrid mode due to transverse velocity shear, *Phys. Fluids* **31**, 2753 (1988).
- [58] H. Romero, G. Ganguli, Y. C. Lee, and P. J. Palmadesso, Electron-ion hybrid instabilities driven by velocity shear in a magnetized plasma, *Phys. Fluids B* **4**, 1708 (1992).
- [59] A. Matsubara and T. Tanikawa, Anomalous cross-field transport of electrons driven by the electron-ion hybrid instability due to the velocity shear in a magnetized filamentary plasma, *Jpn. J. Appl. Phys.* **39**, 4920 (2000).
- [60] T. A. S. Kumar, S. K. Mattoo, and R. Jha, Plasma diffusion across inhomogeneous magnetic fields, *Phys. Plasmas* **9**, 2946 (2002).
- [61] J. Egedal, A. Le, and W. Daughton, A review of pressure anisotropy caused by electron trapping in collisionless plasma, and its implications for magnetic reconnection, *Phys. Plasmas* **20**, 061201 (2013).
- [62] A. Le, J. Egedal, W. Daughton, W. Fox, and N. Katz, Equations of State for Collisionless Guide-Field Reconnection, *Phys. Rev. Lett.* **102**, 085001 (2009).
- [63] G. Ganguli, C. Crabtree, A. C. Fletcher, E. Tejero, D. Malaspina, and I. Cohen, Kinetic equilibrium of dipolarization fronts, *Sci. Rep.* **8**, 17186 (2018).

*Correction:* The quantity  $\hat{L}$  in the seventh paragraph (in “The total electron flow...”) was mistakenly set as  $E_N$  during the production cycle and has been fixed.